Current-induced three-dimensional domain wall propagation in cylindrical NiFe nanowires

Wong, D. W.; Purnama, Indra; Lim, Gerard Joseph; Gan, Wei Liang; Murapaka, Chandra; Lew, Wen Siang

2016

Wong, D. W., Purnama, I., Lim, G. J., Gan, W. L., Murapaka, C., & Lew, W. S. (2016). Current-induced three-dimensional domain wall propagation in cylindrical NiFe nanowires. Journal of Applied Physics, 119(15), 153902-.

https://hdl.handle.net/10356/83556

https://doi.org/10.1063/1.4946753

Current-induced three-dimensional domain wall propagation in cylindrical NiFe nanowires

D. W. Wong, I. Purnama, G. J. Lim, W. L. Gan, C. Murapaka, and W. S. Lew[a)]
School of Physical and Mathematical Sciences, Nanyang Technological University, 21 Nanyang Link, Singapore 637371

(Received 3 February 2016; accepted 1 April 2016; published online 15 April 2016)

We report on the magnetization configurations in single NiFe cylindrical nanowires grown by template-assisted electrodeposition. Angular anisotropic magnetoresistance measurements reveal that a three-dimensional helical domain wall is formed naturally upon relaxation from a saturated state. Micromagnetic simulations support the helical domain wall properties and its reversal process, which involves a splitting of the clockwise and anticlockwise vortices. When a pulsed current is applied to the nanowire, the helical domain wall propagation is observed with a minimum current density needed to overcome its intrinsic pinning. *Published by AIP Publishing.*
[http://dx.doi.org/10.1063/1.4946753]

INTRODUCTION

Ferromagnetic cylindrical nanowires have been proposed as a potential medium for three-dimensional magnetic domain wall (DW)-based memory.[1–3] In such devices, data are stored in the form of two different magnetization directions within the nanowire that are separated by a domain wall. To control the data movement, a spin-polarized current can be used to move the DWs along the nanowire and data between the read and write sensors. The advantage of the three-dimensional memory device over two-dimensional planar memory devices is that a much higher data density can be achieved without compromising the lateral dimension of the memory chip.[4–6] In cylindrical nanowires, different DW types are favored depending on the diameter of the nanowire and the exchange length of the material.[7] At a diameter of 350 nm, a three-dimensional helical DW can be obtained.[8–10] The helical DW is a three-dimensional magnetization configuration that connects clockwise and anticlockwise vortices at the center of the nanowire. Although two-dimensional DWs in planar nanowires have been intensively studied, there are only few experimental studies on three-dimensional DWs in cylindrical nanowires.[10,11]

In this paper, the magnetization reversal in a single cylindrical NiFe nanowire, which occurs via the nucleation of the helical DW and abrupt splitting of the clockwise and anticlockwise vortices, is investigated by anisotropic magnetoresistance measurements (AMR) and micromagnetic simulations. The current-induced DW motion is achieved by injecting pulsed current, which shows relatively high DW speeds, and a minimum current density of $J_{th} = 4.66 \times 10^{12}\,\mathrm{A/m^2}$ is needed to overcome its intrinsic pinning.

METHODOLOGY

Permalloy nanowires were grown using the template-assisted electrodeposition technique at 25 °C in an electrolyte consisting of 0.5M $NiSO_4$, 0.01M $FeSO_4$, and 0.5M H_3BO_3.[11–13] To ensure good conductivity, an aluminum layer was deposited on one side of the Whatman Anodisc anodized aluminum oxide (AAO) template via thermal evaporation before the electrodeposition process. The nanowires were then released by dissolving the AAO template in 1M NaOH solution and thoroughly rinsed with deionized water to de-alkalize. The nanowires had an average diameter of 350 nm, as characterized by scanning electron microscopy (SEM) and a composition of $Ni_{80}Fe_{20}$ as measured by energy dispersive X-ray (EDX). To fabricate the single nanowire device for electrical characterizations, the nanowires were drop casted on Si/SiO_2 substrates, after which lithography was used to form the patterned contact pads. A clean interface was obtained by reverse-sputtering the substrate before the deposition of the adhesion layer (5 nm of Cr) and the metal film (350 nm of Au). The SEM image of the device along with the schematic of the AMR measurement is shown in Figure 1(a). All measurements were performed with a low reading bias current density $J = 1.03 \times 10^9\,\mathrm{A/m^2}$ to avoid joule heating or electron migration.

The magnetization configurations of the nanowires were investigated by means of the Object Oriented Micromagnetic Framework (OOMMF).[14] The material parameters used in the simulations correspond to Permalloy ($Ni_{80}Fe_{20}$), i.e., saturation magnetization $M_s = 860 \times 10^3\,\mathrm{A/m}$, exchange stiffness constant $A_{ex} = 1.3 \times 10^{-11}\,\mathrm{J/m}$, magnetocrystalline anisotropy $k = 0$, Gilbert damping constant $\alpha = 0.005$, and non-adiabatic constant $\beta = 0.04$–0.15.[8,15–19] The helical DW dynamics does not show any significant difference for all β values considered. A 350-nm-diameter cylindrical nanowire with a length of 2 μm was used, and a unit cell size of 5 nm × 5 nm × 5 nm was chosen for all simulations.[8,9]

RESULTS AND DISCUSSION

The magnetoresistance of single NiFe cylindrical nanowires was measured at 300 K. The nanowire is first magnetized and saturated along the axis of interest with an external

[a)]Author to whom correspondence should be addressed. Electronic mail: wensiang@ntu.edu.sg

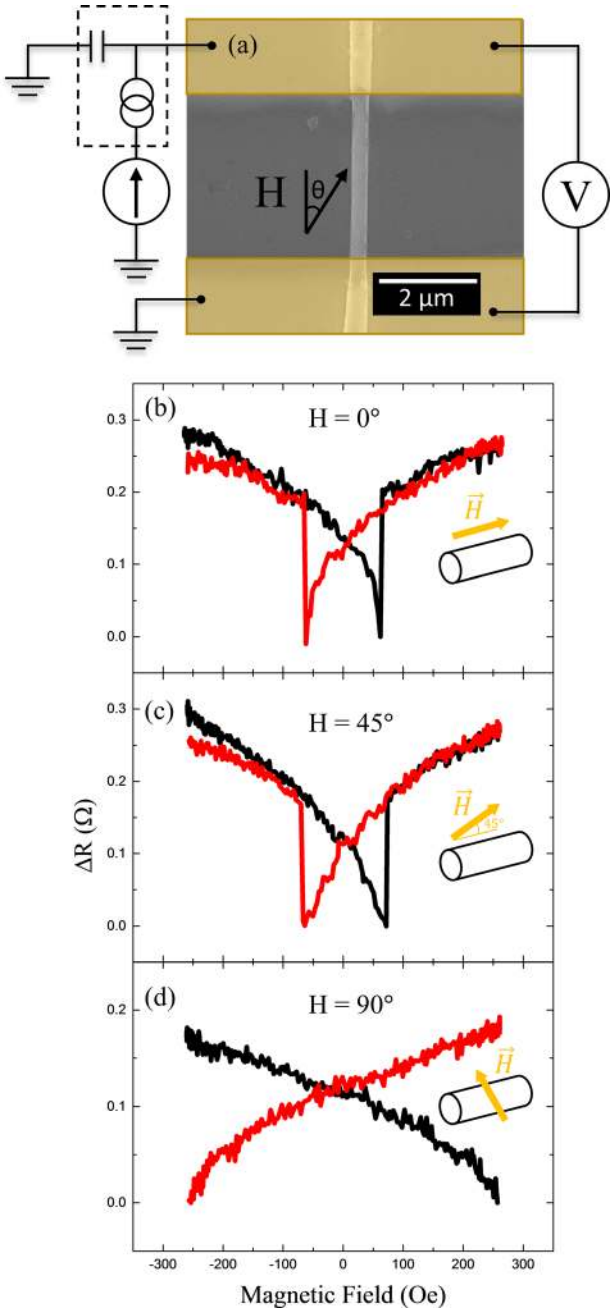

FIG. 1. (a) SEM image of a 350-nm-diameter cylindrical nanowire and set of Au contacts, with schematics of AMR measurement setup. AMR is plotted as a function of the angle between the applied field and the nanowire at (b) 0°, (c) 45°, and (d) 90°. The AMR shows the magnetization reversal in a single cylindrical NiFe nanowire, which occurs via the nucleation of the helical DW and abrupt splitting of the clockwise and anticlockwise vortices.

field of 3 kOe. The samples were then rotated with respect to the direction of applied magnetic field H to obtain the angular dependence of the magnetoresistance. Figures 1(b)–1(d) show the magnetoresistance curves at three different angles ($\theta = 0°$, 45°, and 90°) between the applied magnetic field H and the nanowire long axis. The magnetoresistance of the nanowire measured during the field up-sweep (from –265 Oe to +265 Oe) and down-sweep (from +265 Oe to –265 Oe) is shown by the black and red solid lines, respectively. The magnetoresistance exhibits jumps at low fields (~64 Oe) for both parallel ($\theta = 0°$) and oblique ($\theta = 45°$) applied magnetic fields, whereas at $\theta = 90°$, the magnetoresistance does not show any sudden jumps up to $H = 250$ Oe. The measured magnetoresistance at $\theta = 45°$ is also found to decrease more slowly than that of the parallel magnetic field ($\theta = 0°$) at a field range of between –110 Oe and +100 Oe.

Figure 2(a) shows the extracted up-sweep magnetic field AMR from Figure 1(b); the inset shows the measurements of ΔR in a series of experiments in which the nanowire is initially saturated ($\Delta R = 0$), as compared to the remanence state. To understand the magnetization configurations of the nanowire during the magnetic reversal, micromagnetic simulations were performed, and the results for various magnetization configurations (I–VI) are presented. In the micromagnetic simulations, the nanowire is first saturated in the $-x$ direction parallel to the nanowire long axis (I), as shown in Figure 2(b). As the applied magnetic field is

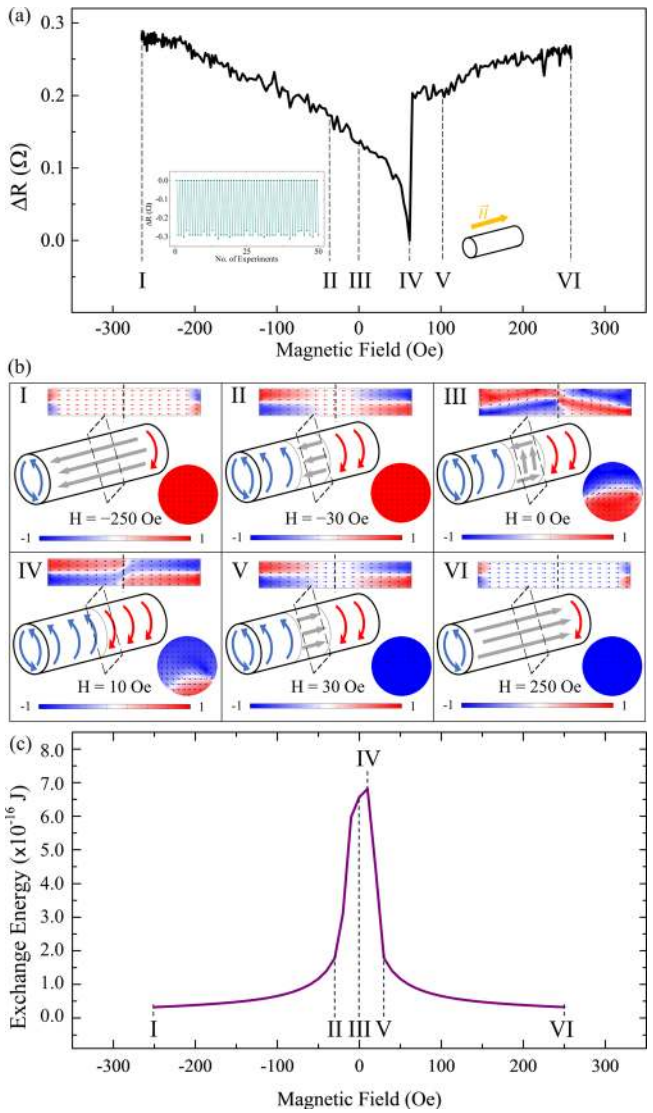

FIG. 2. (a) Up-sweep magnetic field AMR at $\theta = 0°$ applied magnetic field; the inset shows the measurements of ΔR in a series of experiments in which the nanowire is initially saturated ($\Delta R = 0$) and a DW is subsequently nucleated by an applied field. (b) Magnetization configurations of the nanowire at various magnetic field strengths from −265 Oe to +265 Oe. The arrows illustrate the direction of magnetizations, and the colors red and blue represent the clockwise and anticlockwise vortices, respectively. (c) The plot of exchange energy against $\theta = 0°$ applied magnetic field.

reduced, a clockwise and an anticlockwise vortex are nucleated at the ends of the nanowire, which start to move toward the center of the nanowire, leading to a gradual reduction of the parallel magnetization component that causes a drop in the magnetoresistance (II). At 0 Oe (III), a helical DW[8,9] is found to be nucleated when the two vortices meet at the center of the nanowire. As the magnetic field direction is reversed, the helical DW is annihilated at $H \approx -10$ Oe. Next, an abrupt splitting of the two vortices is observed, which leads to a sharp increase in the parallel magnetization component and also the magnetoresistance (IV-V). The magnetoresistance of the nanowire returns to its initial value (VI) as the nanowire begins to saturate in the $+x$ direction. Figure 2(c) shows the plot of exchange energy against parallel magnetic field ($\theta = 0°$), where the sharp drop in exchange energy at IV-V corresponds to the abrupt splitting of the two vortices.

The pinning of DW in cylindrical nanowires is investigated by introducing modulations along the nanowires. In diameter-modulated cylindrical nanowires, the point within the nanowire, where the diameters differ, acts as a pinning site. Figure 3(a) shows the SEM image of the device along with the schematic for AMR measurement. The magnetoresistance jump due to the abrupt switching of the magnetization is observed to occur at a higher field of $H \approx +125$ Oe as compared to an unmodulated nanowire, as shown in Figure 3(b). This magnetization configuration in the diameter-modulated cylindrical nanowires was also examined by micromagnetic simulations, as shown in Figure 3(c). Initially, the diameter-modulated nanowire is saturated in the $-x$ direction parallel to the nanowire long axis (I). The clockwise and anticlockwise vortices start to move towards the thicker region of the nanowire, which similarly leads to a reduction in the parallel magnetization component and causes a drop in magnetoresistance (II). The helical DW is then formed in the thicker region of the nanowire at $H = 0$ Oe (III). As the magnetic field direction is reversed, the helical DW is annihilated. Next, the abrupt splitting of the two vortices is also observed, which leads to an abrupt increase in the parallel magnetization component and also in the magnetoresistance (IV-V). As the nanowire begins to saturate in the $+x$ direction, the magnetoresistance of the nanowire returns to its initial value (VI). In addition, micromagnetic simulation results reveal that the switching field of the cylindrical nanowire increases when the difference in the diameter of the nanowire, Δd, is larger, as shown in Figure 3(d). The increase in the switching field shows that the pinning strength of the modulation increases with increasing Δd, and this phenomenon is also observed in planar nanowires.[20]

The current-induced helical DW motion is examined by introducing a pulsed current generator into the AMR measurement setup, as shown in the inset of Figure 4(a). Initially, a helical DW was nucleated at the center of the nanowire by an up-sweep magnetic field along the nanowire long axis. Subsequently, a 10-ns-long current pulse with a variable amplitude and polarity was applied, while the resistance of the nanowire was measured under a bias current of $J = 1.03 \times 10^9$ A/m^2. The rise and fall time of the current pulse were 300 ps. Figure 4(a) shows that the

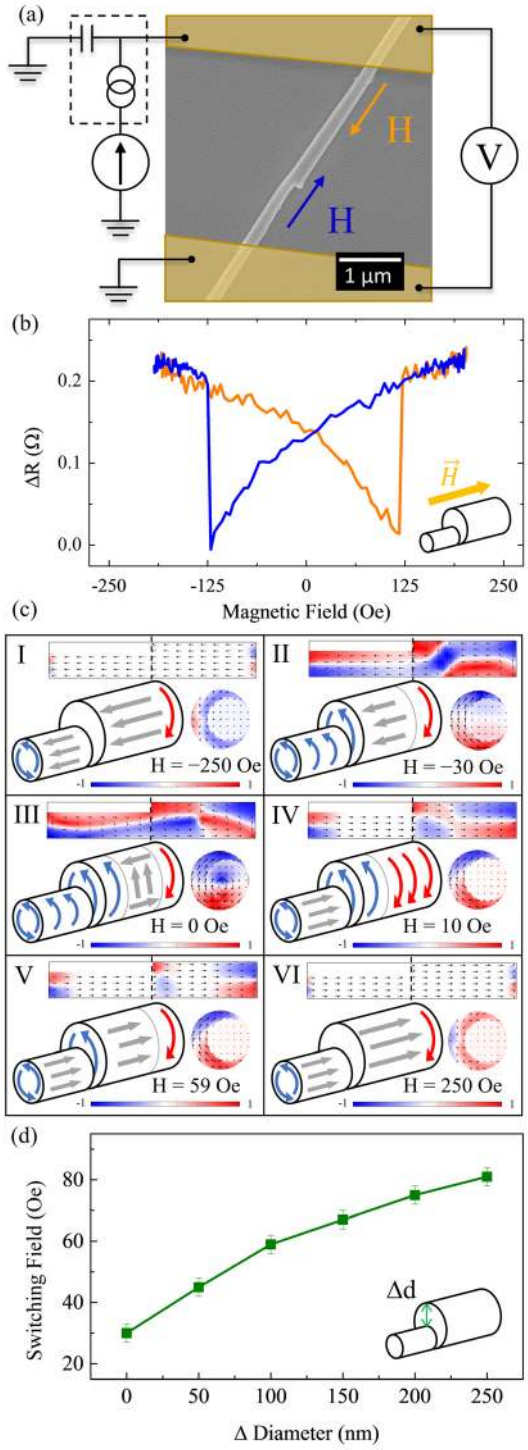

FIG. 3. (a) SEM image of a diameter-modulated 350-nm-diameter cylindrical nanowire and set of Au contacts, with schematics of AMR measurement setup. (b) AMR at $\theta = 0°$ applied magnetic field for a diameter-modulated cylindrical nanowire. (c) Magnetization configurations of the nanowire at various magnetic field strengths. The arrows illustrate the direction of magnetizations, and the colors red and blue represent the clockwise and anticlockwise vortices, respectively. (d) The plot of switching field against $\theta = 0°$ applied magnetic field obtained by micromagnetic simulations.

resistance of the nanowire drops drastically after the application of a pulse current, and Figure 4(b) shows the magnetization configurations of the nanowire, as revealed by micromagnetic simulations, before and after the

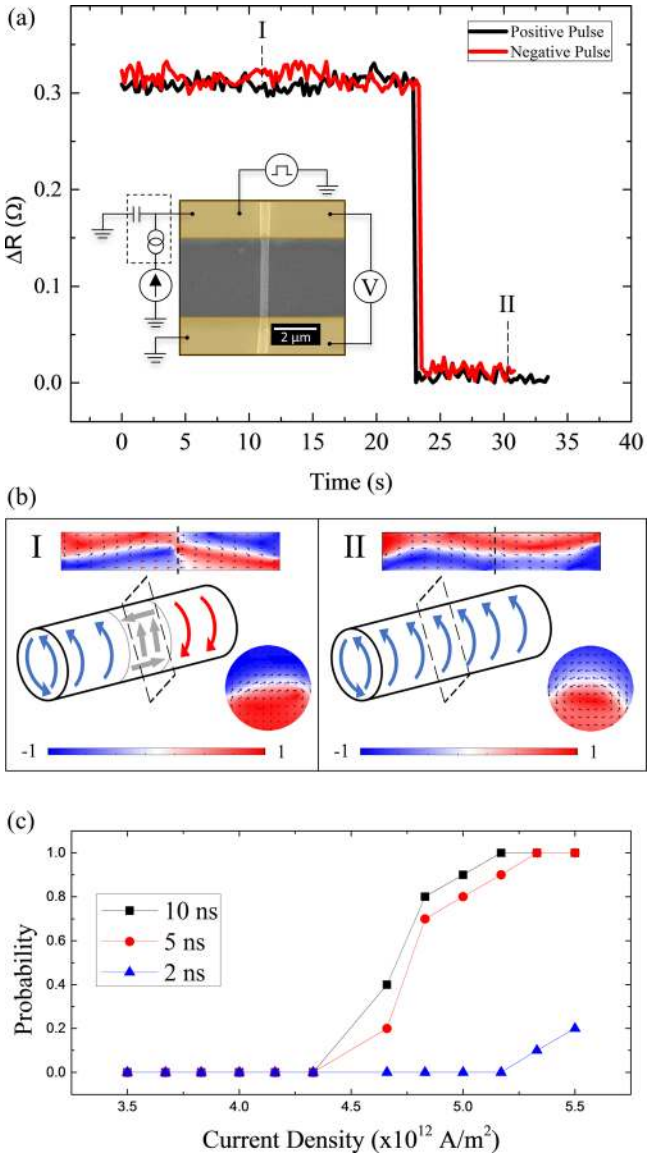

FIG. 4. (a) AMR showing DW motion by the injection of a pulsed current. Inset shows the SEM image of a 350-nm-diameter cylindrical nanowire and set of Au contacts, with schematics of AMR measurement setup. (b) Magnetization configurations of the cylindrical nanowire corresponding to the states before and after DW driving. The arrows illustrate the direction of magnetizations, and the colors red and blue represent the clockwise and anticlockwise vortices, respectively. (c) The driving probability of the DW as a function of current density for a range of pulsed durations (2 ns, 5 ns, and 10 ns).

application of the pulse current. The results show the current-induced magnetization configuration of the nanowire, where the helical DW is driven to the end of the nanowire, which differs from the field-induced dynamics that shows the abrupt splitting of the vortices. As the helical DW is pushed out by the injected current pulse, a single vortex magnetization configuration is formed throughout the nanowire. The magnetization state (II) as shown by the micromagnetic simulation is expected to have a lower magnetoresistance, as the magnetization configuration within the nanowire is more uniform, as compared to the initial state (I) where a helical DW is present.

Figure 4(c) shows the probability (P) at which a drop in resistance was observed against the applied current density for various pulse durations (2 ns, 5 ns, and 10 ns). $P = 1$ means that the helical DW is always driven to the end of the nanowire by the current pulse. To obtain the probability, each measurement was repeated 50 times. The results show that, at applied current densities $J > 4.66 \times 10^{12}$ A/m^2, there is a gradual increase in probability from 0 to 1 for the 5 ns and 10 ns pulse durations. The probability for the 2 ns pulse duration remains relatively low, even with increasing current densities. This minimum current density needed to overcome the intrinsic pinning of the helical DW is found to be $J_{th} = 4.66 \times 10^{12}$ A/m^2. In our previous micromagnetic studies,[8] the calculated minimum current density (J_i) for the helical DW to overcome its intrinsic pinning in a smooth cylindrical nanowire was found to be $J_i = 5.0 \times 10^{11}$ A/m^2. The higher minimum current density ($J_{th} > J_i$) can be attributed to the lower mobility arising from the surface roughness, which contributes to the viscous damping of the DW motion.[21,22] It is then possible to obtain the helical DW velocity as a function of the applied current density by noting the lowest current at which $P = 1$. In our experimental results, the helical DW velocity was found to be ~158 m/s for a 10 ns pulse at $J_{10\,ns} = 5.17 \times 10^{12}$ A/m^2 and ~317 m/s for a 5 ns pulse at $J_{5\,ns} = 5.33 \times 10^{12}$ A/m^2.

CONCLUSION

In summary, Permalloy ($Ni_{80}Fe_{20}$) cylindrical nanowires were fabricated using the template-assisted electrodeposition technique. AMR measurements and micromagnetic simulations reveal that the magnetization reversal of a single cylindrical nanowire occurs via the nucleation of a helical DW and is followed by the abrupt splitting of the clockwise and anticlockwise vortex. The injection of pulsed current allows the driving of the helical DW with a speed of up to 317 m/s, while a minimum current density of $J_{th} = 4.66 \times 10^{12}$ A/m^2 is needed to overcome its intrinsic pinning.

ACKNOWLEDGMENTS

This work was supported by the Singapore National Research Foundation, Prime Minister's Office, under a Competitive Research Programme (Non-volatile Magnetic Logic and Memory Integrated Circuit Devices, NRF-CRP9-2011-01). WSL is a member of the Singapore Spintronics Consortium (SG-SPIN). We also wish to acknowledge the funding for this project from Nanyang Technological University under the Undergraduate Research Experience on CAmpus (URECA) programme.

[1]M. Yan, A. Kákay, S. Gliga, and R. Hertel, Phys. Rev. Lett. **104**, 057201 (2010).
[2]G. S. D. Beach, M. Tsoi, and J. L. Erskine, J. Magn. Magn. Mater. **320**, 1272–1281 (2008).
[3]M. Chandra Sekhar, S. Goolaup, I. Purnama, and W. S. Lew, J. Appl. Phys. **115**, 083913 (2014).
[4]S. S. P. Parkin, M. Hayashi, and L. Thomas, Science **320**, 190–194 (2008).
[5]S. Parkin and S.-H. Yang, Nat. Nanotechnol. **10**, 195–198 (2015).
[6]M. Hayashi, L. Thomas, C. Rettner, R. Moriya, X. Jiang, and S. S. P. Parkin, Phys. Rev. Lett. **97**, 207205 (2006).
[7]R. Wieser, U. Nowak, and K. D. Usadel, Phys. Rev. B **69**, 064401 (2004).
[8]D. W. Wong, M. Chandra Sekhar, W. L. Gan, I. Purnama, and W. S. Lew, J. Appl. Phys. **117**, 17A747 (2015).

[9]M. Chandra Sekhar, H. F. Liew, I. Purnama, W. S. Lew, M. Tran, and G. C. Han, Appl. Phys. Lett. **101**, 152406 (2012).
[10]N. Biziere, C. Gatel, R. Lassalle-Balier, M. C. Clochard, J. E. Wegrowe, and E. Snoeck, Nano Lett. **13**, 2053–2057 (2013).
[11]M. S. Salem, P. Sergelius, R. M. Corona, J. Escrig, D. Gorlitz, and K. Nielsch, Nanoscale **5**, 3941–3947 (2013).
[12]W. L. Gan, M. Chandra Sekhar, D. W. Wong, I. Purnama, S. Y. Chiam, L. M. Wong, and W. S. Lew, Appl. Phys. Lett. **105**, 152405 (2014).
[13]A. Pereira, J. L. Palma, M. Vazquez, J. C. Denardin, and J. Escrig, Phys. Chem. Chem. Phys. **17**, 5033–5038 (2015).
[14]M. J. Donahue and D. G. Porter, Interagency Report No. NISTIR 6376 (National Institute of Standards and Technology, Gaithersburg, MD, 1999).
[15]L. Thomas, M. Hayashi, X. Jiang, R. Moriya, C. Rettner, and S. S. Parkin, Nature **443**, 197–200 (2006).
[16]M. L. Schneider, T. Gerrits, A. B. Kos, and T. J. Silva, Appl. Phys. Lett. **87**, 072509 (2005).
[17]M. Eltschka, M. Wötzel, J. Rhensius, S. Krzyk, U. Nowak, M. Kläui, T. Kasama, R. E. Dunin-Borkowski, L. J. Heyderman, H. J. van Driel, and R. A. Duine, Phys. Rev. Lett. **105**, 056601 (2010).
[18]L. Heyne, J. Rhensius, D. Ilgaz, A. Bisig, U. Rüdiger, M. Kläui, L. Joly, F. Nolting, L. J. Heyderman, J. U. Thiele, and F. Kronast, Phys. Rev. Lett. **105**, 187203 (2010).
[19]S. D. Pollard, L. Huang, K. S. Buchanan, D. A. Arena, and Y. Zhu, Nat. Commun. **3**, 1028 (2012).
[20]J. Akerman, M. Muñoz, M. Maicas, and J. L. Prieto, Phys. Rev. B **82**, 064426 (2010).
[21]V. O. Dolocan, Appl. Phys. Lett. **105**, 162401 (2014).
[22]G. S. Beach, C. Nistor, C. Knutson, M. Tsoi, and J. L. Erskine, Nat. Mater. **4**, 741–744 (2005).